Sustainable Materials and Technologies 40 (2024) e00925

Contents lists available at ScienceDirect

Sustainable Materials and Technologies

journal homepage: www.elsevier.com/locate/susmat

3D-honeycomb architectures evaporator toward mutual reinforcement of evaporation and catalysis for efficient freshwater harvesting

Yi Zhang [a,b], Peng Xiao [b,c], Jincui Gu [b,c,*], Wenqin Wang [a,**], Tao Chen [b,c,*]

[a] School of Materials Science and Chemical Engineering, Ningbo University, Ningbo 315211, China
[b] Key Laboratory of Marine Materials and Related Technologies, Zhejiang Key Laboratory of Marine Materials and Protective Technologies, Ningbo Institute of Material Technology and Engineering, Chinese Academy of Science, Ningbo 315201, China
[c] College of Material Chemistry and Chemical Engineering, Key Laboratory of Organosilicon Chemistry and Material Technology, Ministry of Education, Hangzhou Normal University, Hangzhou 311121, Zhejiang, People's Republic of China.

ARTICLE INFO

Keywords:
Honeycomb architecture
Interfacial solar-driven evaporation
LDH nanoflower
Advanced catalytic oxidation
Mutual reinforcement

ABSTRACT

Solar-driven freshwater harvesting has emerged as an effective and sustainable technology to mitigate global water scarcity due to its high energy conversion efficiency. Nevertheless, achieving mutual reinforcement of photothermal and photocatalysis processes is in high demand because the contamination of harmful and highly concentrated volatile organic compounds (VOCs) will inevitably evaporate and condense alongside water. Herein, an integrated 3D-honeycomb fabric (NPPF) evaporator decorated with polydopamine (PDA), polypyrrole (PPy), and hydrotalcite (LDH) nanoflowers was designed innovatively by synergistically cooperating photothermal evaporation and advanced catalytic oxidation techniques. With periodically concave arrays, it can create the maximum level of light-trapping through multiple scattering and omnidirectional light absorption, thereby increasing its photothermal catalytic degradation ability. Meanwhile, introducing the LDH nanoflowers boosted the photothermal evaporation capacity of the NPPF evaporator. Therefore, it demonstrated high solar absorption efficiency of ~98.02% and an evaporation rate of ~2.02 kg m^{-2} h^{-1} under one sun. Furthermore, it can achieve superb degradation activity, especially for high-concentration VOCs, with efficiency of ~93.99%, surpassing most of the other evaporators reported previously. Besides, the outdoor experiment demonstrated its practicability. More importantly, it can remove tetracycline and phenol with efficiency of ~98.85% and ~ 92.06%. The advantages make this evaporator a promising representative for cooperative freshwater production.

1. Introduction

Due to limited water resources, population growth and climate change, freshwater scarcity has become a global challenge to sustainable development [1,2]. Solar-thermal interfacial water harvesting technology has recently provided an integrated solution to obtain clean water concurrently and alleviate water shortage [3–5]. So far, pioneering explorations have focused on achieving high solar conversion efficiency, including constructing rational architectures for water regulation, light-to-heat conversion enhancement, and solar absorbers heat management, and impressive achievements have been achieved [4–15]. However, some organic pollutants, especially volatile organic compounds (VOCs), will evaporate with the water, leading to secondary pollution and restricting the practicability of solar-driven interfacial evaporation [16–21]. In addition, the non-VOCs will be concentrated and resulted in the blocked evaporation. Therefore, it is difficult to treat complex sewage containing organic pollutants to minimize energy consumption and environmental impact.

Designing a multifunctional evaporator integrated with a photocatalytic process provides an excellent inspiration for removing VOCs during solar-thermal interfacial evaporation [22–26]. For example, Yan et al. displayed an integrated graphene oxide-based aerogel for freshwater production from complex wastewater. It can achieve an evaporation rate of ~2.08 kg m^{-2} h^{-1} and the VOCs (10 ppm) remove efficiency of ~94.8% [22]. Zhou et al. showed organic-inorganic nanocomposites to achieve pollutant removal and clean water

* Corresponding authors at: Key Laboratory of Marine Materials and Related Technologies, Zhejiang Key Laboratory of Marine Materials and Protective Technologies, Ningbo Institute of Material Technology and Engineering, Chinese Academy of Science, Ningbo 315201, China.
** Corresponding author.
E-mail addresses: gujincui@nimte.ac.cn (J. Gu), wangwenqin@nbu.edu.cn (W. Wang), tao.chen@nimte.ac.cn (T. Chen).

https://doi.org/10.1016/j.susmat.2024.e00925
Received 18 February 2024; Received in revised form 21 March 2024; Accepted 6 April 2024
Available online 9 April 2024

production simultaneously. It can reach a water-vapor generation ability of 1.41 kg m^{-2} h^{-1} and > 95% removal of pollutants under one sun [23]. These works present an alternative solution to develop a sustainable and integrated photothermal process for freshwater production. Despite these achievements, due to the small penetration depth of light, most often suffers from hinder the integrated use of solar energy, thereby balancing the synergy of interfacial evaporation and photocatalytic decontamination remains a grand challenge [27–30].

Encouragingly, the emerging advanced oxidation process, mainly activated peroxymonosulfate (PMS), with merits of high selectivity, high redox potential and long half-life, has recently aroused colossal interest [31–35]. Generally, the catalysts can produce various reactive oxygen species (ROS), such as hydroxyl (•OH), sulfate (SO_4•$^-$), superoxide radicals (•O_2^-), and nonradicals such as singlet oxygen ($^1O_2$), activated by thermal energy, ultraviolet irradiation, and so on [32,33]. Considering that interfacial solar evaporators can realize photothermal conversion, the localized heat produced from the photothermal materials can synergistically accelerate the active sites of catalysts to produce ROS to degrade pollutants [36–40]. Therefore, introducing advanced activating PMS heterogeneous catalysts into the interfacial solar evaporation will simultaneously realize the integration of solar evaporation and catalytic degradation. Nevertheless, the previous materials suffer from low activation efficiency for highly concentrated VOCs [41–45]. Therefore, developing a bifunctional evaporator well-integrated with excellent photothermal-catalytic properties is the core but has not been thoroughly studied.

Layered double hydroxide (LDH) is a promising alternative for photocatalysis and photothermal due to its characteristics of unique intercalation structure, abundant hydroxyl group on the laminate, and flexible and adjustable metal site, bandgap tuning, compositional diversity, and controllable particle size [46–48]. Herein, a novel LDH nanoflowers decorated 3D-honeycomb fabric evaporator (NPPF) was designed by functionalizing polydopamine (PDA) and polypyrrole (PPy) (Fig. 1a). The 3D honeycomb fabric in the NPPF evaporator presented a periodic concave array structure to capture the light and recycle the convective and radiative heat, and the layered structure of the hydrotalcite nanoflowers can promote the multiple scattering and omnidirectional light and enhance the light path length to harvest internal light absorption (Fig. 1b). Furthermore, introducing LDH can enhance the light absorption performance of the NPPF evaporator. Consequently, under one sun, this evaporator showed a high solar efficiency of ~98.02% and an rate of ~2.02 kg m^{-2} h^{-1}.

Besides, due to the appropriate bandgap of the LDH nanoflowers (~2.18 eV, Fig. S1), it can achieve superb degradation activity, especially for high-concentration VOCs, with efficiency of ~93.99%, outperforming most of the reported evaporators (Fig. 1c-d). An outdoor experiment demonstrated that the total water production reached ~10.50 kg m^{-2}, and the TC and phenol removal efficiency got ~98.85% and ~ 92.06%. The distinctive advantages of this evaporator make it a promising representative for cooperative freshwater production and pollutant remediation.

2. Experiment

2.1. Materials

The honeycomb fabric was purchased from the Hebei Orui Textile Technology Co., LTD. LDH nanoflowers were obtained from the Science Compass Research Service Center. Dopamine hydrochloride, hydrochloric acid (HCl, 37%), tris- (hydroxymethyl) aminomethane (Tris), ferric chloride ($FeCl_3$·$6H_2O$), pyrrole, chloroform, sodium polyacrylate (PAANa, Mw =80,000–90,000 M) were purchased from Sigma-Aldrich Co. Ltd. Peroxymonosulfate ($KHSO_5$•$0.5KHSO_4$•$0.5K_2SO_4$, PMS), rhodamine B (RhB), Tetracycline (TC), methylene blue (MB), bisphenol A (BPA) and phenol was supplied by Sigma-Aldrich Co. Ltd. Others were bought from Sigma-Aldrich Co. Ltd.

2.2. Preparation of evaporators with 3D-honeycomb and plane structure, respectively

The NPPF was prepared through multi-step interface assembly. Firstly, the honeycomb fabric (F) was ultrasonicated with ethanol to remove different adsorbates. Secondly, the fabric was immersed into the dopamine solution (pH = 8.5, 10 mmol/L, 1 M Tris-HCl) for 12 h, then

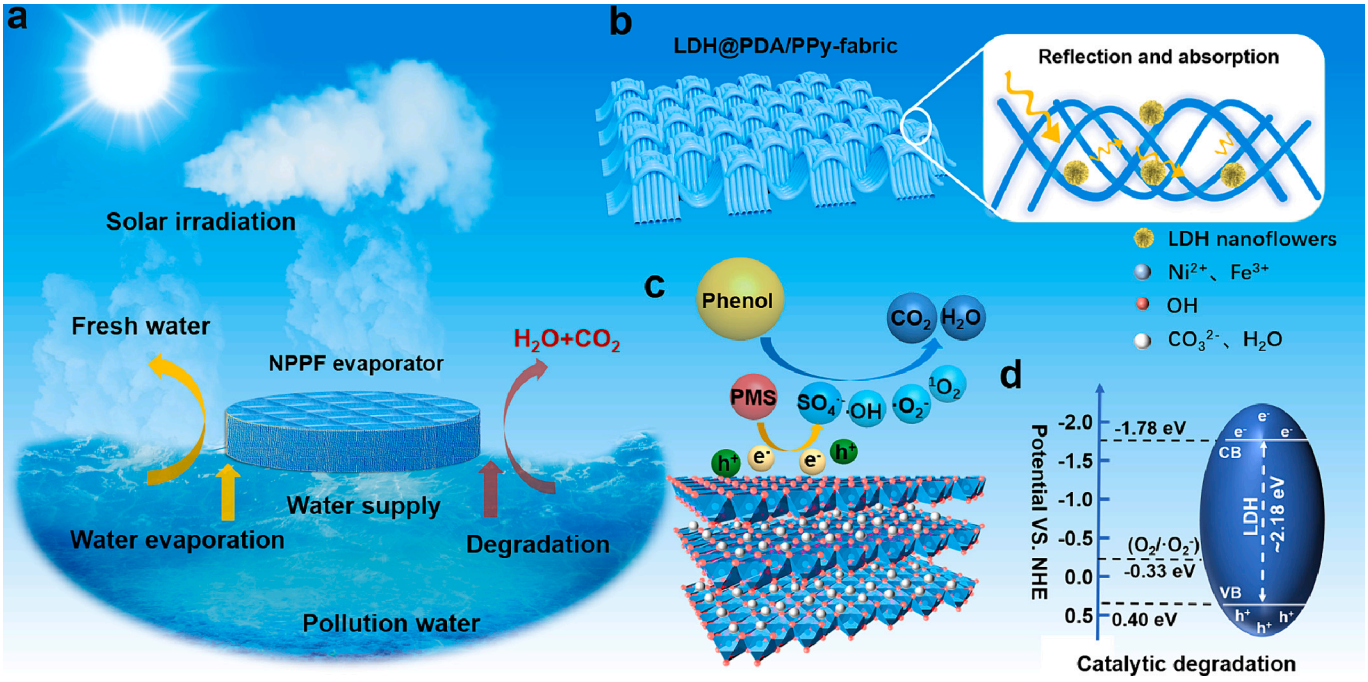

Fig. 1. (a) Schematic illustration of the NPPF evaporator for photothermal evaporation and advanced catalytic oxidation degradation. (b) The NPPF evaporator can improve photothermal conversion efficiency through multiple scattering and omnidirectional light to harvest internal light absorption. (c) Mechanism diagram of the catalytic degradation of the LDH nanoflower during the photothermal evaporation. (d) Energy diagram and band position of the LDH nanoflower.

rinsed with deionized water and dried under 60 °C for 2 h to get the PDA functionalized fabric (PDA/fabric) (PF). Thirdly, the PF was immersed into the $FeCl_3{\cdot}6H_2O$ solution (0.5 mol/L) for 1.5 h and then thoroughly into the pyrrole/chloroform mixture (0.2 mol/L) for 0.5 h, and was washed with water to remove Fe^{3+}/Fe^{2+} and dried in an oven for 2 h. The PPy functionalized PF (PPF) was obtained. Afterwards, the PPF was soaked in sodium polyacrylate aqueous solution (1 g/L) for 5 min then dried for 1 h. Lastly, different amounts of the LDH nanoflower (5–25 mg) dispersions was sprayed onto the PDA/PPy-fabric and dried at 60 °C for 3 h to obtain LDH@PDA/PPy-fabric, which labelled as NPPF-5, NPPF-10, NPPF-15, NPPF-20, NPPF-25, respectively. Similarly, the evaporators with planar structures were also constructed for comparison experiments, including plane fabric and plane PPy-fabric, labelled P-fabric and PPP, respectively.

2.3. Characterization

The morphology information of different fabrics was got from the field emission scanning electron microscope (FE-SEM, Hitachi-S4800, Japan). Energy-dispersive X-ray spectroscopy (EDS, Thermo Scientific, USA) was used to observe the samples' chemical composition and elemental maps. The crystal property was collected from the X-ray diffractometer using a Cu target (XRD, Panalytical Germany) with rate of 5°/min and 2θ =10–80° (λ = 1.5406 Å). The ultraviolet-visible-near-infrared spectrophotometer (UV–vis-IR, Lambda 950, America) was used to measure the absorption spectra of different fabrics and the bandgap of the LDH nanoparticles. X-ray photoelectron spectroscopy (XPS, Axis Ultra DLD, England) was used to analyze different fabrics' chemical composition. The Mott-Schottky curve test of the LDH nanoflowers was carried out on the electrochemical workstation (CHI750, China). Fourier transform infrared (FTIR, Cary660 + 620, America) spectrometer was used to test the chemical constituents. The contact angle of water droplets was measured on the contact angle meter (OCA-20, America). Room temperature electron paramagnetic resonance (EPR, EMXplus-6/1, Germany) was used to detect the active species during the illumination. The IR thermal camera was used to capture the thermal image temperatures (Optris pi 400, Japan). Inductively coupled plasma atomic emission spectroscopy (ICP-AES, NexION 300×, Japan) was used to analyze the concentrations of ions in the water.

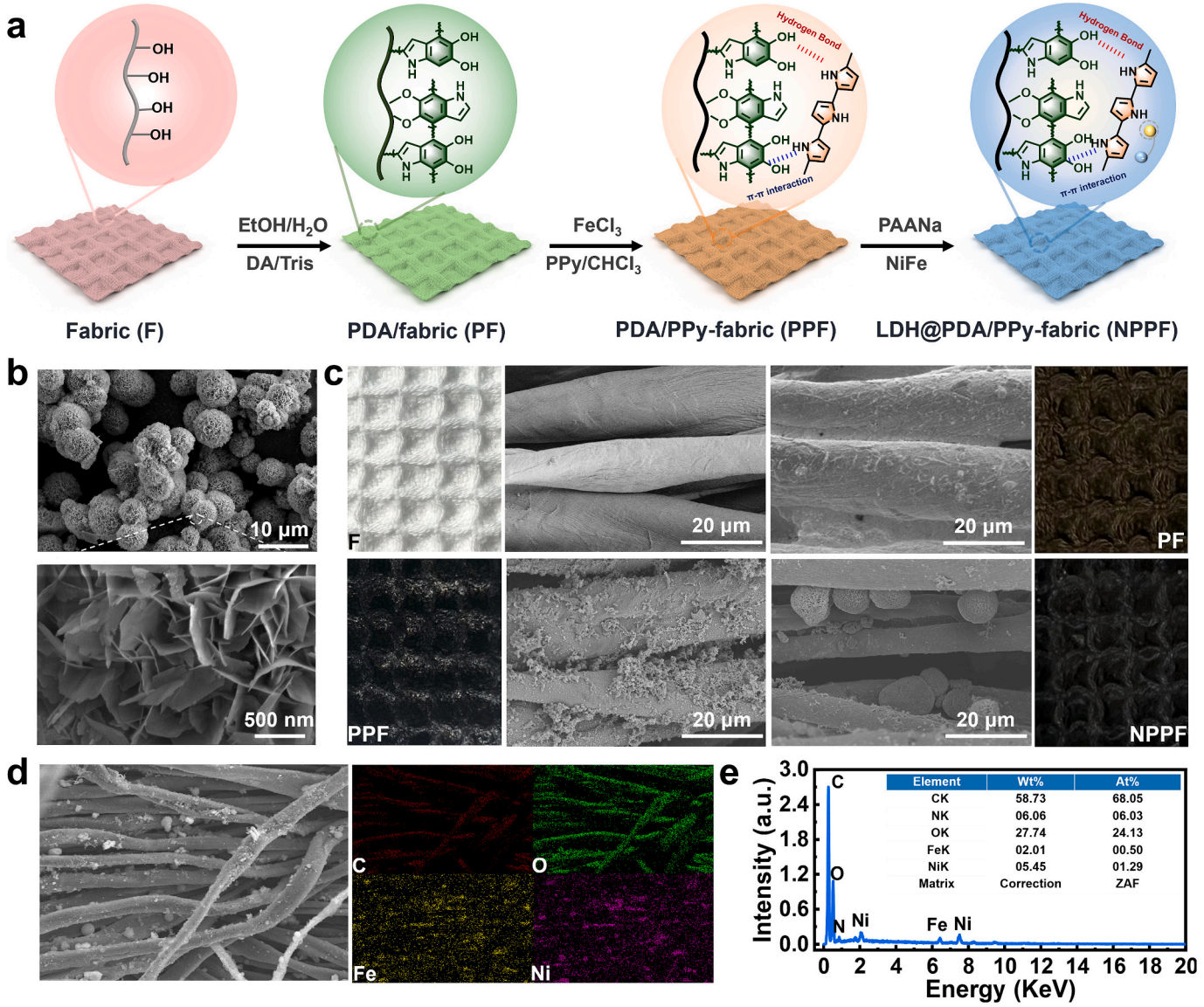

Fig. 2. (a) Schematic illustration of the preparation of the NPPF evaporator through the multi-step interface assembly. (b) SEM and its responding enlarged images of the LDH nanoflowers. (c) Photographs and SEM images of the F, PF, PPF and NPPF, respectively. (d) SEM and the responding energy spectrum of the NPPF. (e) EDS result of the element content of the NPPF.

3. Results and discussion

The 3D honeycomb-structured NPPF evaporator was fabricated by a self-assembly strategy. As illustrated in Fig. 2a, the F was modified with dopamine to get the PF. The abundant phenolic hydroxyl and amino groups of dopamine endowed the PF with a platform for engineering functionalization [49,50]. Moreover, introducing the PDA will enhance the photoconversion performance of the PF due to the high molar extinction coefficient of the PDA molecules. Subsequently, the PPy molecular chains were in-situ functionalized on the surface of the PF to obtain the PPF through the multiple hydrogen bonding and π-π conjugation effects. Due to the excellent photothermal conversion performance and low thermal conductivity of PPy, the incorporation of PPy will make the PPF an ideal lightweight and efficient photothermal conversion material [51,52]. Finally, the LDH nanoflowers were self-assembled on the PAANa functionalized PPF to obtain the NPPF via the electrostatic interaction (Fig. S2).

The LDH nanoflowers micromorphology was surveyed in detail through SEM. The average size of LDH nanoflowers was ~5.39 μm with a petaloid microstructure and substantial wrinkles morphology (Fig. 2b, S3). The rough structure of LDH nanoflowers can promote its effective contact with contaminations, giving the NPPF evaporator remarkable catalytic degradation performance and boosting the light absorption capacity through multiple internal reflections [53,54]. Then, the macro- and micro-structures of the fabric before and after modification were studied. As displayed in Fig. 2c, the raw fabric was white and presented a smooth fibrous structure. After the PDA and PPy interface functionalization, the fabric became dark, and abundant folds and rough microspheres were formed (Fig. S4). This was the joint effect of the encapsulation of polymer molecular chains and the hydrophobicity of pyrrole molecules. After the interface assembly of the LDH nanoflowers, numerous particles were uniformly anchored on the surface or embedded into the interior of the PPF fiber, as proved by the homogeneous element distribution in the EDS (Fig. S5, 2d-2e), laying the foundation for collaborative photothermal evaporation and photocatalysis.

The chemical information of the NPPF was characterized systematically through XRD. Fig. S6 showed apparent characteristic peaks at

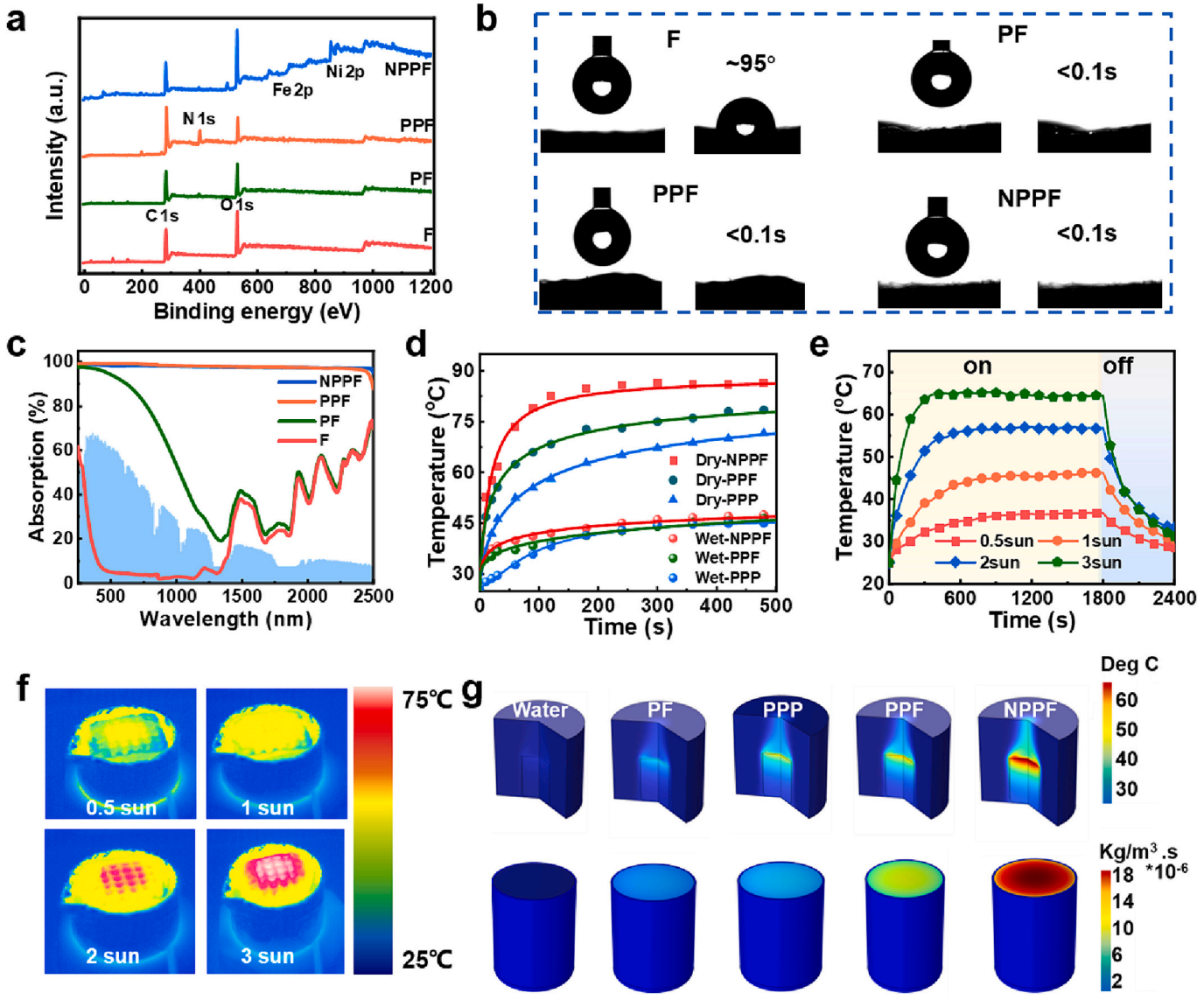

Fig. 3. (a) XPS spectra of the F, PF, PPF and NPPF, respectively. (b) WCA of the F, PF, PPF and NPPF, respectively. (c) UV–Vis-IR spectra of F, PF, PPF and NPPF (wavelength of 400– 2500 nm) compared with the standard filter (blue). (d) The temperature curves of the PPP, PPF and NPPF with different states under one sun irradiation. (e) The temperature curves of the NPPF with different states under different suns irradiation. (f) The IR thermal images of NPPF under different suns irradiation. (g) COMSOL simulation of the pure water, PF, PPP, PPF and NPPF with regard to temperature (upper) and evaporation changes (bottom), respectively.

~11.50°, ~23.33°, and ~ 34.64°, evidencing to the typical peak of the (003), (006) and (012) [55]. According to the Bragg formula ($2d\sin\theta = \lambda$), the layer spacing was ~0.792 nm, ~0.394 nm, and ~ 0.261 nm, respectively. The good multiples of lattice spacing also indicated that the hydrotalcite formed an ideal microscopic layered structure in the LDH nanoflowers. More importantly, the characteristic peaks of the LDH nanoflowers can also be observed in the NPPF, suggesting that the functionalization of the PDA and PPy had little influence on the LDH nanoflowers. It was beneficial to exert the catalytic degradation performance of the LDH nanoflowers to a greater extent.

Furthermore, XPS was carried out to explore the chemical information of these fabrics. As displayed in Fig. 3a, the C and O elements occurred in the raw fabric. After modifying the PDA and PPy, the N element peak appeared at ~401.5 eV in the PPF. Moreover, the new peaks that appeared at ~712.9 eV and ~ 856.1 eV were respective to the Fe 2p and Ni 2p spectrum of the NPPF. The Fe 2p signal peaks were divided into ~711.5 eV and ~ 725.4 eV, respectively, attributed to the Fe 2p3/2 and Fe 2p1/2 of Fe^{3+} (Fig. S7a) [56]. Meanwhile, the Ni 2p spectrum was split into two peaks at 857.0 eV and 876.2 eV, corresponding to the Ni 2p3/2 and Ni 2p1/2 of Ni^{2+} (Fig. S7b) [56]. FTIR and WCA were further carried out to verify the formation of each sample. As described in Fig. S6, the weak absorption peaks at ~1156 cm^{-1}, ~1276 cm^{-1}, ~1529 cm^{-1}, and ~ 1028 cm^{-1} represented the C-N stretching vibration and five-element ring expansion of the PPy (Fig. S8). Moreover, the enhancement absorption peaks at ~3300 cm^{-1} and ~ 1351 cm^{-1} stood for the -OH group stretching vibration and asymmetric stretching vibration peak of CO_3^{2-}, indicating the introduction of the LDH nanoflowers [57]. Furthermore, the fabric became superhydrophilic after collaborating with PDA, PPy, and LDH nanoflowers because of the abundant hydroxyl functional groups (Fig. 3b, Movie S1-S4). The strong pumping ability of the NPPF could obtain sufficient water molecules to match the evaporation rate, which is favorable for the subsequent photothermal evaporation.

The light absorb capacity is crucial to determine the solar-to-thermal conversion efficiency. As shown in Fig. 3c, the PF showed ~60.45% absorption of total solar energy (wavelength of 400–2500 nm). However, after the functionalization of the PPy, the light absorption capacity was significantly enhanced to ~97.88% due to the excitation and vibration of electrons in PPy molecules. More importantly, the absorb light ability synergistically increased to ~98.02% after assembling the LDH nanoflowers due to the multiple transmission/ reflection in the NPPF with honeycomb arrays (Fig. S9). The ΔT difference between the initial and equilibrated temperatures can reflect the photothermal conversion ability. As reflected in Fig. 3d, the surface temperature of the NPPF evaporator with wet or dry states increased from 25.0 to 45.5 °C and 25.0 to 86.5 °C under one sun irradiation, respectively, which was significantly higher than that of the PF, PPF, and PPP evaporators, further demonstrating the synergistic light absorption enhancement ability of LDH nanoflowers and honeycomb architectural structure. The thermal localization ability under different sun irradiation was studied in detail. As shown in Fig. 3e-3f, with the solar illumination in light on and off modes, the temperature of the NPPF evaporator changed simultaneously. When the solar intensity gradually increased from 0.5 to 3, the surface temperatures stabilized within 5 min, demonstrating the fast response and excellent photothermal property of NPPF evaporator.

A COMSOL simulation heat transfer model was also implemented to explain the heat transfer process. The simulation models were created based on the actual experimental conditions to investigate the transient heat transfer process and the temperature distribution of the evaporator (detailed discussion in Section S2). As illustrated in Fig. 3g, the surface temperature of the NPPF evaporator was distinctly higher than the other evaporators, including the PF evaporator, PPP evaporator, and PPF evaporator, which was well agreed with the experimental results. This was because multiple reflections and incident light absorption occurred among the NPPF fabrics with periodic arrays of concave patterns. Besides, there was a temperature difference between the top surfaces and insides due to the disparity in solar light intensity from the surface geometry [58,59].

Furthermore, the solar-to-thermal efficiencies (η) of the F, PF, PPF, NPPF were calculated. As shown in Fig. 4a, the η of NPPF was ~89.41%, superior to the F (~20.20%), PF (~48.65%), PPF (~88.97%) under one sun. The enhanced efficiency of NPPF benefited from the following factors: 1) multiple diffuse reflections and low heat loss (Fig. 4b, Section S3), 2) increased specific surface area, 3) synergistic light absorption properties from PPy and LDH nanoflower. Therefore, the NPPF evaporator presented a giant potential to enhance its mutual reinforcement of evaporation and catalysis via optimizing its architectural structure. Given the excellent solar-to-thermal property of the NPPF evaporator, a homemade real-time solar evaporation system was designed to calculate the water evaporation performance, and the schematic diagram is displayed in Fig. 4c. The NPPF evaporator presented a rate of ~2.02 kg m^{-2} h^{-1}, which was higher than that of the F evaporator (~0.67 kg m^{-2} h^{-1}), PF evaporator (~1.16 kg m^{-2} h^{-1}), PPF evaporator (~1.74 kg m^{-2} h^{-1}), and was consistent with the COMSOL simulation of the pure water, PF, PPF and NPPF concerning evaporation changes (Fig. 3g). Similarly, the evaporation rates of the F evaporator and PPF evaporator were approximately ~1.3 times of the evaporation rate of the P-fabric evaporator (~0.51 kg m^{-2} h^{-1}) and PPP evaporator (~1.33 kg m^{-2} h^{-1}) (Fig. 4d). The solar evaporation efficiency was calculated to evaluate each evaporator's energy utilization capacity. As displayed in Fig. 4e, the evaporation efficiency of the NPPF evaporator was as high as ~118.93%, which was ~1.8 times of the PPF evaporator (~101.31%) and much larger than that of the other evaporators. The excellent solar evaporation efficiency of the NPPF evaporator was owing to the cooperative effect of its honeycomb structure and LDH nanoflowers assembly. For one thing, the temperature difference between the bottom and insides can produce thermocapillary force or temperature gradient-induced Marangoni effect, which can facilitate the evaporation performance of the NPPF evaporator [60]. For another, the introduction of the LDH nanoflowers can improve the thermal management of NPPF evaporators, thus enabling more efficient heat utilization.

The evaporation rate of the NPPF can be controlled by adjusting the contents of the LDH nanoflowers. As shown in Fig. 4f, the evaporation rate gradually enhanced with the increased amounts of the LDH nanoflowers. However, excess LDH nanoflowers (25 mg) may lead to lower photothermal conversion capacity and unnecessary heat conduction inside the NPPF evaporator, resulting in a decline of evaporation rate. Consequently, the LDH (20 mg) exhibited the maximum evaporation rate (~2.02 kg m^{-2} h^{-1}), approximately 3.3 times larger than pure water. Besides, the evaporation rate of the NPPF-20 evaporator can be adjusted by controlling the solar intensity to acquire evaporation rates of ~0.75 kg m^{-2} h^{-1}, ~2.74 kg m^{-2} h^{-1}, ~5.17 kg m^{-2} h^{-1} under the irradiation of 0.5, 2.0, 3.0 suns, respectively (Fig. 4g). More importantly, the NPPF-20 evaporator demonstrated excellent evaporator performance even under cyclic and high light irradiation (Fig. 4h). Besides, it was noteworthy that this evaporator exhibited outstanding evaporation performance for TC, RhB, MB, and BPA solutions (100 ppm) with evaporation rates of ~1.98 kg m^{-2} h^{-1}, ~1.97 kg m^{-2} h^{-1}, ~1.97 kg m^{-2} h^{-1}, ~1.98 kg m^{-2} h^{-1}, respectively (Fig. 5a), suggesting the excellent universality of the NPPF-20 evaporator.

The catalytic degradation of contaminants is imperious demands to avoid the second pollution. Here, the antibiotic TC was selected as the model pollutant to assess the photocatalytic performance of the NPPF-20 evaporator. As shown in Fig. 5b and S10, the NPPF-20 evaporator almost reached adsorption equilibrium within 10 min in darkness. This evaporator could not efficiently degrade TC solution with an efficiency of ~35.14% under one sun irradiation. By contrast, the photocatalytic efficiency of the NPPF-20 evaporator increased to ~98.16% with the aid of PMS. Furthermore, the effect of concentration of the PMS on catalytic degradation performance was studied. As shown in Fig. S11, when the concentration was increased to 2.5 mmol/L, the degradation efficiency of the TC could reach up to ~100%. The rate constant (k) of TC was

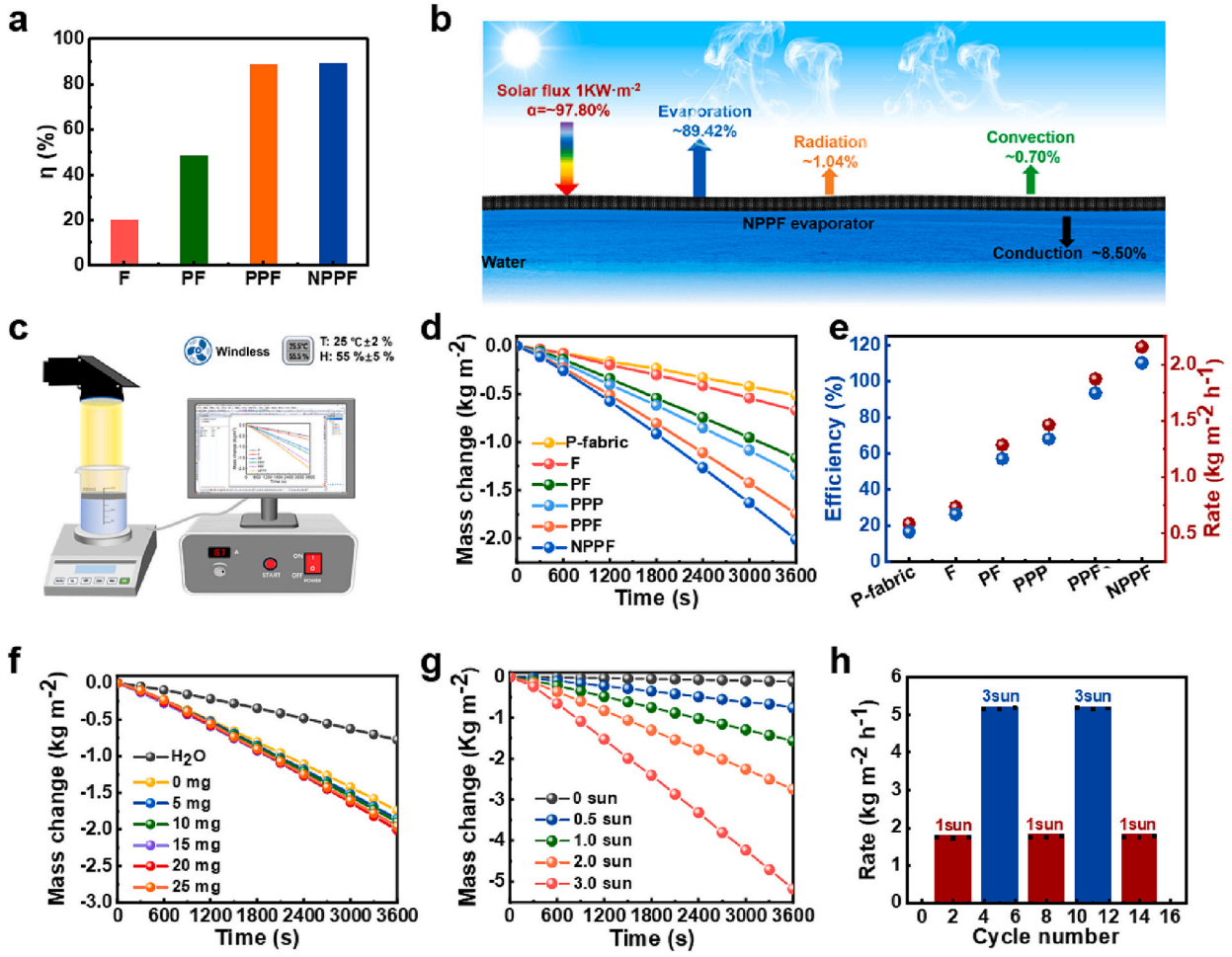

Fig. 4. (a) The photothermal conversion efficiency of the F, PF, PPF, NPPF, respectively. (b) The calculated data of the heat loss of the NPPF under one sun irradiation. (c) The schematic diagram of interface photothermal evaporation. (d) The mass changes of the P-fabric, PPP, F, PF, PPF, NPPF, respectively. (e) The evaporation efficiency and rates of the P-fabric, PPP, F, PF, PPF, NPPF, respectively. (f) The mass changes of the NPPF with different LDH contents. (g) The mass changes of the NPPF-20 under different suns irradiation. (h) The cyclic evaporation rate of the NPPF-20 for water under different suns irradiation.

calculated using the pseudo-first-order kinetics formula. As displayed in Fig. 5c, the k of TC in the NPPF-20 + PMS (~0.182 min^{-1}) was ~36 times that of the NPPF-20, certifying that the thermal energy and visible light effectively activated the NPPF-20 + PMS. In addition, the k of BPA and MB were much lower than TC and RhB, because the BPA and MB possess more stable benzene ring structures compared to TC and RhB. Furthermore, the NPPF-20 + PMS evaporator maintained its catalytic performance after five cycles (Fig. S13). Notably, the NPPF-20 + PMS evaporator showed excellent photocatalytic degradation for other contaminants (100 ppm), including BPA, MB and RhB, with efficiency of ~99.97%, ~99.99%, and ~ 99.99% (Fig. 5d) and k of ~0.015 min^{-1}, ~0.049 min^{-1}, ~0.242 min^{-1}, respectively (Fig. 5e). After degradation, the solutions become almost colorless with the efficiency of ~98.75%, ~98.78%, and ~ 99.89%, respectively (Fig. 5f, S11). The NPPF-20 + PMS evaporator presented a remarkable photocatalytic degradation capacity for phenol with an efficiency of ~95.99% (Fig. 5f). The powerful and universal catalytic performance of the NPPF-20 + PMS evaporator was due to ROS through the ERP test. As exhibited in Fig. 5g, the four-line signal and the six-line signal were attributable to •OH adduct and $SO_4^{\bullet-}$ adduct, respectively. Moreover, the peak intensity of •OH adduct was slightly higher than that of the $SO_4^{\bullet-}$ adduct, confirming the transformation from $SO_4^{\bullet-}$ adduct to •OH adduct. In addition, the intense signal with ratio of 1:1:1 can also be observed, indicating that $\bullet O_2^-$ was generated during the degradation process (Fig. 5h). Besides, consecutive peaks were monitored, belonging to $^1O_2$ adduct (Fig. 5i) [61,62]. Noticeably, no signals were observed in the pure PMS system. Compared with this, these signals were generated from the PMS decomposition. As consequence, it can be deduced that the $^1O_2$ and $SO_4^{\bullet-}$, •OH, $\bullet O_2^-$ were generated in the NPPF-20 + PMS system, which was produced by the iron oxidation variation in NPPF-20 [62].

The probable mechanism of the synergetic reinforcement of solar-driven evaporation and catalytic degradation of phenol of the NPPF-20 evaporator was proposed (Fig. 5j). On the one hand, due to the introduction of the LDH nanoflowers, the NPPF-20 evaporator demonstrated excellent photothermal conversion ability and fast water transport behavior. On the other hand, the NPPF-20 evaporator with a periodically concave array structure could optimally expose abundant surface catalytic sites of LDH nanoflowers. The localized thermal energy stemming from the interfacial solar-driven evaporation can effectively promote the PMS activation. During this process, the HSO_5^- reacted with the Ni^{2+} and Fe^{3+} to generate $SO_4^{\bullet-}$, OH^-, $SO_5^{\bullet-}$, and H^+ (formula 1–2). Afterward, the as-generated $SO_4^{\bullet-}$ reacted with water and produced ·OH (formula 3). Subsequently, $O_2^{\bullet-}$ was generated by the SO_5^{2-} reaction with water, and $^1O_2$ was produced through HSO_5^- with SO_5^{2-} (formula 4–5). Meanwhile, the LDH nanoflowers were excited under sunlight irradiation, stimulating photoinduced electron (e^-) and positive hole (h^+). The generated e^- was captured with PMS to produce $SO_4^{\bullet-}$, and the h^+ participated in the degradation of the contaminant. In a word, the collaboration of the produced active free radical ($SO_4^{\bullet-}$, $\bullet OH^-$, $O_2^{\bullet-}$, $^1O_2$) and h^+ efficiently contributed to the catalytic degradation of the

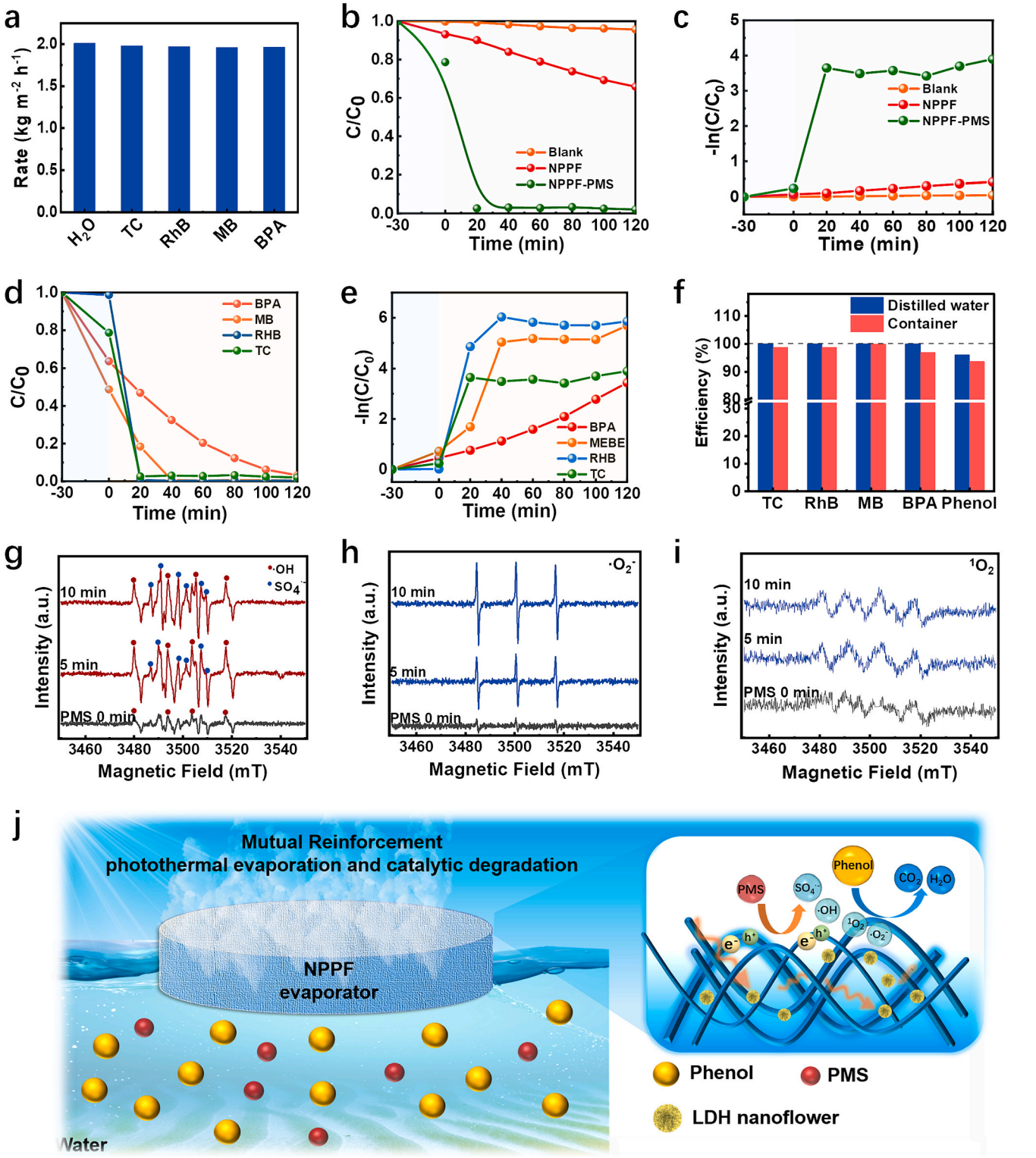

Fig. 5. (a) Evaporation rates of the NPPF-20 evaporator under one sun irradiation for different contaminants, including TC, RhB, MB, and BPA solution (100 ppm). (b-c) The catalytic activities of NPPF, PMS solution, and NPPF-20 + PMS for TC solution under one sun irradiation. (d-e) The catalytic activities of NPPF-20 + PMS for different contaminants under one sun irradiation. (f) Catalytic degradation efficiency of the NPPF-20 + PMS for different contaminants under one sun irradiation. (g-i) EPR tests for free radical trapping of NPPF-20 evaporator with the aid of PMS or not. (j) Catalytic degradation mechanism of the NPPF-20 + PMS evaporator.

contaminants into CO_2, H_2O, and others [63,64]. Accordingly, the NPPF-20 evaporator demonstrated outstanding catalytic degradation capacity for different pollutions, especially for highly concentrated VOCs (100 ppm), with an efficiency of ~99.9%, exceeding most of the reported integrated evaporators (Fig. 6a, Table S1) [65–68].

$$Ni^{2+} + HSO_5^- \rightarrow Ni^{3+} + SO_4^{\bullet -} + OH^- \quad (1)$$

$$Fe^{3+} + HSO_5^- \rightarrow Fe^{2+} + SO_5^{\bullet -} + H^+ \quad (2)$$

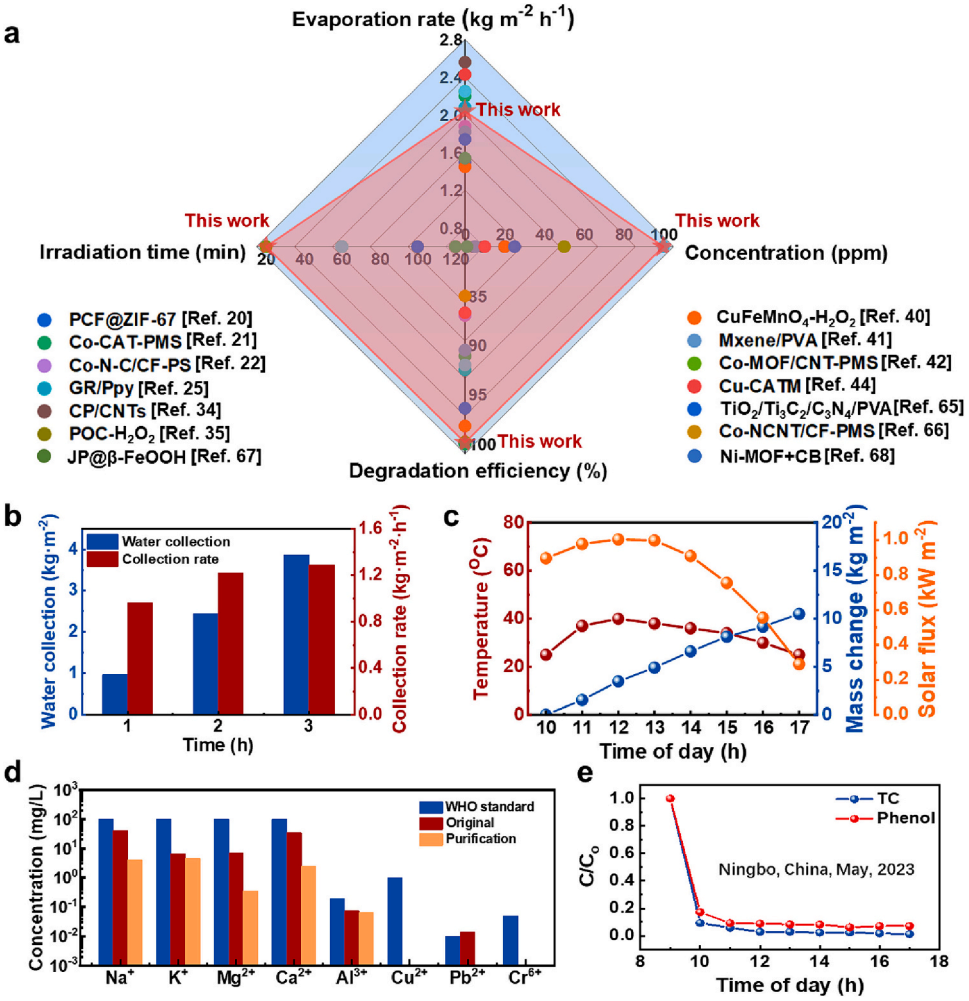

Fig. 6. (a) The comparison of different previous evaporations reported and this work for their Photothermal evaporation and catalytic degradation performances. (b) The water collection and collection rates of different hours of the NPPF-20 evaporator. (c) The mass change of the NPPF-20 evaporator with the change of the outdoor temperature and light intensity (Ningbo, China, May 1, 2023). (d) Ion contents in the seawater before and after the evaporation of the NPPF-20 evaporator. (e) The degradation efficiency of the NPPF-20 for TC and phenol.

$$SO_4^{\bullet-} + H_2O \rightarrow SO_4^{2-} + \bullet OH + H^+ \quad (3)$$

$$SO_5^{2-} + H_2O \rightarrow SO_4^{2-} + H^+ + O_2^{\bullet-} \quad (4)$$

$$HSO_5^- + SO_5^{2-} \rightarrow SO_4^{2-} + HSO_4^- + {}^1O_2 \quad (5)$$

An outdoor experiment was carried out to explore the practicability of the NPPF evaporator concerning its synergetic interfacial solar-driven generation and catalytic degradation. The device was placed from 10:00–17:00. As shown in Fig. S12 and Section S6, the water droplets can be observed distinctly on the condenser within one hour. Moreover, the water collection rate gradually increased, and 3.86 g of water could be collected after three hours (Fig. 6b). Furthermore, maximal solar intensity and surface temperature can reach 0.998 kW m^{-2} and 41.0 °C, respectively. Hence, the highest water production rate and the total water production of the NPPF-20 evaporator arrived at 1.74 kg m^{-2} h^{-1} and 10.50 kg m^{-2} within six hours, respectively (Fig. 6c). In addition, the NPPF-20 evaporator can remove various ions during the interfacial solar-driven generation process. As shown in Fig. 6d, all the ion concentrations (including the heavy metal ions) after purification reached the World Health Organization (WHO) standards for drinking water. Last, the TC and phenol removal efficiency reached ~98.85% and ~92.06% after seven hours, illustrating the good catalytic properties of the NPPF-20 evaporator (Fig. 6e). The above achievements indicated the potential application of the NPPF-20 evaporator for freshwater production.

4. Conclusion

A novel NPPF evaporator with honeycomb architecture was developed for enhanced freshwater production. The periodically concave arrays of this evaporator and the introduction of LDH nanoflowers can generate a good solar efficiency of up to ~98.02% through multiple scattering and omnidirectional light absorption. Therefore, it can achieve an excellent evaporation rate of ~2.02 kg m^{-2} h^{-1} under one sun illumination. More surprisingly, cooperating solar-to-thermal conversion capacity with abundant catalytic sites of the LDH nanoflowers, the NPPF evaporator could effectively activate PMS and achieve a superb degradation activity for various contaminants, especially for high-concentration VOCs, with efficiency of ~93.99%, transcending most the other integrated evaporators reported previously. Given this, the outdoor experiment displayed the photothermal evaporation and catalytic degradation for TC and phenol with efficiency of ~98.85% and ~92.06%, respectively, unambiguously indicating its feasibility for simultaneous polluted water remediation and clean water production. This NPPF evaporator will lay the foundation to mutually reinforce photothermal evaporation and catalysis degradation to address freshwater scarcity.

Supplementary data to this article can be found online at https://doi.

org/10.1016/j.susmat.2024.e00925.

CRediT authorship contribution statement

Yi Zhang: Methodology, Data curation, Investigation. **Peng Xiao:** Investigation, Data curation. **Jincui Gu:** Editing, Supervision, Writing origin manuscript. **Wenqin Wang:** Characterization, Writing origin manuscript. **Tao Chen:** Writing-review, Supervision, Conceptualization.

Declaration of competing interest

None.

Data availability

Data will be made available on request.

Acknowledgment

This work was supported by National Key Research and Development Program (2022YFC2805202), Natural Science Foundation of China (52373094), Ningbo Natural Science Foundation (2022J286), Ningbo Science and Technology Bureau (2021Z127).

References

[1] M.M. Mekonnen, A.Y. Hoekstra, Four billion people facing severe water scarcity, Sci. Adv. 2 (2016) e1500323, https://doi.org/10.1126/sciadv.1500323.
[2] P. Tao, G. Ni, C.Y. Song, W. Shang, J.B. Wu, J. Zhu, G. Chen, T. Deng, Solar-driven interfacial evaporation, Nat. Energy 3 (12) (2018) 1031–1041, https://doi.org/10.1038/s41560-018-0260-7.
[3] L. Zhou, X. Li, G.W. Ni, S. Zhu, J. Zhu, The revival of thermal utilization from the sun: interfacial solar vapor generation, Natl. Sci. Rev. 6 (3) (2019) 562–578, https://doi.org/10.1093/nsr/nwz030.
[4] Y.X. Zhang, T. Xiong, D.K. Nandakumar, S.C. Tan, Structure architecting for salt-rejecting solar interfacial desalination to achieve high-performance evaporation with in situ energy generation, Adv. Sci. 7 (9) (2020) 1903478, https://doi.org/10.1002/advs.201903478.
[5] C.J. Chen, Y.D. Kuang, L.B. Hu, Challenges and opportunities for solar evaporation, Joule 3 (3) (2019) 683–718, https://doi.org/10.1016/j.joule.2018.12.023.
[6] F. Zhao, Y.H. Guo, X.Y. Zhou, W. Shi, G.H. Yu, Materials for solar-powered water evaporation, Nat. Rev. Mater. 5 (5) (2020) 388–401, https://doi.org/10.1038/s41578-020-0182-4.
[7] Y.H. Guo, F. Zhao, X.Y. Zhou, Z.C. Chen, G.H. Yu, Tailoring nanoscale surface topography of hydrogel for efficient solar vapor generation, Nano Lett. 19 (4) (2019) 2530–2536, https://doi.org/10.1021/acs.nanolett.9b00252.
[8] Z.H. Li, M.X. Wang, L.M. Chen, H.B. Ji, H.Y. Yu, Highly efficient carbonization of nanocellulose to biocarbon aerogels with ultrahigh light absorption efficiency and evaporateion rate as bifunctional solar/electric driven steam generator for water purification, Sustain. Mater. Technol. 36 (2023) e00649, https://doi.org/10.1016/j.susmat.2023.e00649.
[9] D. Wei, C. Wang, J. Zhang, H. Zhao, Y. Asakura, M. Eguchi, X. Xu, Y. Yamauchi, Water activation in solar-powered vapor generation, Adv. Mater. 35 (2023) 2212100, https://doi.org/10.1002/adma.202212100.
[10] D. Wei, C. Wang, G. Shi, J. Zhang, F. Wang, P. Tan, Z. Zhao, Y. Xie, Enabling self-adaptive water-energy-balance of photothermal water diode evaporator: dynamically maximizing energy utilization under the ever-changing sunlight, Adv. Mater. (2024) 2309507, https://doi.org/10.1002/adma.202309507.
[11] C. Wang, K. Xu, G. Shi, D. Wei, Water skin effect and arched double-sided evaporation for boosting all-weather high salinity desalination, Adv. Energy Mater. 13 (2023) 2300134, https://doi.org/10.1002/aenm.202300134.
[12] K. Xu, C. Wang, Z. Li, S. Wu, J. Wang, Salt mitigation strategies of solar-driven interfacial desalination, Adv. Funct. Mater. 31 (2021) 2007855, https://doi.org/10.1002/adfm.202007855.
[13] Z. Wu, D. Sun, C. Shi, S. Chen, S. Tang, Y. Li, C. Yan, Y. Shi, B. Su, Moisture-thermal stable, superhydrophilic alumina-based ceramics fabricated by a selective laser sintering 3D printing strategy for solar steam generation, Adv. Funct. Mater. 33 (2023) 2304897, https://doi.org/10.1002/adfm.202304897.
[14] Y. Li, P. Chen, Z. Wu, C. Shi, P. Chen, Y. Xu, X. Chen, M. Chen, Y. Li, C. Yan, Y. Shi, B. Su, A nonradiographic strategy to real-time monitor the position of three-dimensional-printed medical orthopedic implants by embedding superparamagnetic Fe_3O_4 particles, Interdiscip. Mater. 3 (2024) 133–149, https://doi.org/10.1002/idm2.12133.
[15] Y. Xu, S. Zhang, S. Li, Z. Wu, Y. Li, Z. Li, X. Chen, C. Shi, P. Chen, P. Zhang, M. D. Dickey, B. Su, A soft magnetoelectric finger for robots' multidirectional tactile perception in non-visual recognition environments, Npj Flex. Electron. 8 (2024) 2, https://doi.org/10.1038/s41528-023-00289-6.
[16] Y. Chen, S. Fang, L. Sun, F. Xu, M. Wang, J. Zhang, X. Mu, X. Wang, P. Wang, J. Liu, Hierarchical $NiFe_2O_4$-NiAl-LDH arrays immobilized on activated carbon cloth for bifunctional application on high-performance supercapacitors and solar steam generation, Sustain. Mater. Technol. 33 (2022) e00500.
[17] Q.C. Xia, C. Wang, N. Xu, J.H. Yang, G.D. Gao, J. Ding, A floating integrated solar micro-evaporator for self-cleaning desalination and organic degradation, Adv. Funct. Mater. 33 (28) (2023) 2214769, https://doi.org/10.1002/adfm.202214769.
[18] W. Cho, D. Lee, G. Choi, J. Kim, A.E. Kojo, C. Park, Supramolecular engineering of amorphous porous polymers for rapid adsorption of micropollutants and solar-powered volatile organic compounds management, Adv. Mater. 34 (50) (2022) 2206982, https://doi.org/10.1002/adma.202206982.
[19] D.P. Qi, Y. Liu, Y.B. Liu, Z.Y. Liu, Y.F. Luo, H.B. Xu, X. Zhou, J.J. Zhang, H. Yang, W. Wang, X.D. Chen, Polymeric membranes with selective solution-diffusion for intercepting volatile organic compounds during solar-driven water remediation, Adv. Mater. 32 (50) (2020) 2004401, https://doi.org/10.1002/adma.202004401.
[20] H.T. Mo, Y. Wang, A bionic solar-driven interfacial evaporation system with a photothermal-photocatalytic hydrogel for VOC removal during solar distillation, Water Res. 226 (2022) 119276, https://doi.org/10.1016/j.watres.2022.119276.
[21] B. Zhang, P.W. Wong, A.K. An, Photothermally enabled MXene hydrogel membrane with integrated solar-driven evaporation and photodegradation for efficient water purification, Chem. Eng. J. 430 (2022) 133054, https://doi.org/10.1016/j.cej.2021.133054.
[22] S. Yan, H. Song, Y. Li, J. Yang, X. Jia, S. Wang, X. Yang, Integrated reduced graphene oxide/polypyrrole hybrid aerogels for simultaneous photocatalytic decontamination and water evaporation, Appl. Catal. B Environ. 301 (2022) 120820, https://doi.org/10.1016/j.apcatb.2021.120820.
[23] J. Wang, M. Sun, C. Liu, Y. Ye, M. Chen, Z. Zhao, Y. Zhang, X. Wu, K. Wang, Y. Zhou, Customized microenvironments spontaneously facilitate coupled engineering of real-life large-scale clean water capture and pollution remediation, Adv. Mater. 35 (41) (2023) 2306103, https://doi.org/10.1002/adma.202306103.
[24] Y. Peng, X. Wei, Y. Wang, W. Li, S. Zhang, J. Jin, Metal-organic framework composite photothermal membrane for removal of high-concentration volatile organic compounds from water via molecular sieving, ACS Nano 16 (5) (2022) 8329–8337, https://doi.org/10.1021/acsnano.2c02520.
[25] L. Shi, Y. Shi, S. Zhuo, C. Zhang, Y. Aldrees, S. Aleid, P. Wang, Multi-functional 3D honeycomb ceramic plate for clean water production by heterogeneous photo-Fenton reaction and solar-driven water evaporation, Nano Energy 60 (2019) 222–230, https://doi.org/10.1016/j.nanoen.2019.03.039.
[26] Y. Lu, X. Wang, D.Q. Fan, H. Yang, H.L. Xu, H.H. Min, X.F. Yang, Biomass derived Janus solar evaporator for synergic water evaporation and purification, Sustain. Mater. Technol. 25 (2020) e00180, https://doi.org/10.1016/j.susmat.2020.e00180.
[27] D. Hao, Y. Yang, B. Xu, Z. Cai, Bifunctional fabric with photothermal effect and photocatalysis for highly efficient clean water generation, ACS Sustain. Chem. Eng. 6 (8) (2018) 10789–10797, https://doi.org/10.1021/acssuschemeng.8b02094.
[28] R. Niu, Y. Ding, L. Hao, J. Ren, J. Gong, J. Qu, Plant-mimetic vertical-channel hydrogels for synergistic water purification and interfacial water evaporation, ACS Appl. Mater. Interfaces 14 (40) (2022) 45533–45544, https://doi.org/10.1021/acsami.2c14773.
[29] H. Peng, D. Wang, S. Fu, Artificial transpiration with asymmetric photothermal textile for continuous solar-driven evaporation, spatial salt harvesting and electrokinetic power generation, Chem. Eng. J. 426 (2021) 131818, https://doi.org/10.1016/j.cej.2021.131818.
[30] P. Yang, W. Bai, Y. Zou, X. Zhang, Y. Yang, G. Duan, J. Wu, Y. Xu, Y. Li, A melanin-inspired robust aerogel for multifunctional water remediation, Mater. Horiz. 10 (3) (2023) 1020–1029, https://doi.org/10.1039/D2MH01474B.
[31] Y.N. Li, J. Wei, N. Cui, J.M. Li, M.D. Xu, G.P. Pan, Z.J. Jiang, X.R. Cui, X.R. Niu, J. Li, Recent advance of atomically dispersed dual-metal sites carbocatalysts: properties, synthetic materials, catalytic mechanisms, and applications in persulfate-based advanced oxidation process, Adv. Funct. Mater. 33 (30) (2023) 2301229, https://doi.org/10.1002/adfm.202301229.
[32] Y. Zhao, R.C. Zhang, J.M. Huang, Y. Zhang, B. Han, Y.P. Ying, M. Chen, S.Y. Xie, D. M. Chen, Imprinting defective Fe-based metal-organic frameworks as an excellent platform for selective Fenton/persulfate degradation of LEX: removal performance and mechanism, Appl. Catal. B Environ. 337 (2023) 122919, https://doi.org/10.1016/j.apcatb.2023.122919.
[33] R. Djellabi, L. Noureen, V.D. Dao, D. Meroni, E. Falletta, D.D. Dionysiou, C. L. Bianchi, Recent advances and challenges of emerging solar-driven steam and the contribution of photocatalytic effect, Chem. Eng. J. 431 (2022) 134024, https://doi.org/10.1016/j.cej.2021.134024.
[34] L. Cui, P. Wang, H. Che, X. Gao, J. Chen, B. Liu, Y. Ao, Co nanoparticles modified N-doped carbon nanosheets array as a novel bifunctional photothermal membrane for simultaneous solar-driven interfacial water evaporation and persulfate mediating water purification, Appl. Catal. B Environ. 330 (2023) 122556, https://doi.org/10.1016/j.apcatb.2023.122556.
[35] A. Li, J. Xiong, Y. Liu, L. Wang, X. Qin, J. Yu, Fiber-intercepting-particle structured MOF fabrics for simultaneous solar vapor generation and organic pollutant adsorption, Chem. Eng. J. 428 (2022) 131365, https://doi.org/10.1016/j.cej.2021.131365.
[36] D. Li, Z.Q. Liang, H. Yang, M.J. Zhang, K.L. Cao, B. Zhao, Y.W. Wang, M.W. Peng, Y.H. Sun, L. Jiang, Mutual reinforcement of evaporation and catalysis for efficient freshwater-salt-chemical production, Adv. Funct. Mater. 33 (49) (2023) 2300353, https://doi.org/10.1002/adfm.202300353.
[37] S.Y. Dong, Y.L. Zhao, J.Y. Yang, X.D. Liu, W. Li, L.Y. Zhang, Y.H. Wu, J.H. Sun, J. L. Feng, Y.F. Zhu, Visible-light responsive PDI/rGO composite film for the photothermal catalytic degradation of antibiotic wastewater and interfacial water

evaporation, Appl. Catal. B Environ. 291 (2021) 120127, https://doi.org/10.1039/C5TA05002B.
[38] P.P. He, H.Y. Bai, Z.F. Fan, L. Hao, N. Liu, B.Y. Chen, R. Niu, J. Gong, Controllable synthesis of N/Co-doped carbon from metal-organic frameworks for integrated solar vapor generation and advanced oxidation processes, J. Mater. Chem. A 10 (25) (2022) 13378–13392, https://doi.org/10.1039/D2TA02767D.
[39] M. Ikram, M. Rashid, A. Haider, S. Naz, J. Haider, A. Raza, M.T. Ansar, M.K. Uddin, N.M. Ali, S.S. Ahmed, M. Imran, S. Dilpazir, Q. Khan, M. Maqbool, A review of photocatalytic characterization, and environmental cleaning, of metal oxide nanostructured materials, Sustain. Mater. Technol. 30 (2021) e00343, https://doi.org/10.1016/j.susmat.2021.e00343.
[40] X. Zhao, Y. Jiang, T. Wang, Q. Lu, K. Zhao, J. Pan, Photothermal-photocatalytic route of MOF-based membrane with nanosheet array structures for solar-driven water purification, Chem. Eng. J. 475 (2023) 146268, https://doi.org/10.1016/j.cej.2023.146268.
[41] P.P. He, H.Y. Lan, H.Y. Bai, Y.Y. Zhu, Z.F. Fan, J. Liu, L.J. Liu, R. Niu, Z.Y. Dong, J. Gong, Rational construction of "all-in-one" metal-organic framework for integrated solar steam generation and advanced oxidation process, Appl. Catal. B Environ. 337 (2023) 123001, https://doi.org/10.1016/j.apcatb.2023.123001.
[42] L.F. Cui, C.F. Ma, P.F. Wang, H.N. Che, H.L. Xu, Y.H. Ao, Rationally constructing a 3D bifunctional solar evaporator for high-performance water evaporation coupled with pollutants degradation, Appl. Catal. B Environ. 337 (2023) 122988, https://doi.org/10.1016/j.apcatb.2023.122988.
[43] J. Li, L. Ding, Z. Su, K. Li, F. Fang, R. Sun, Y. Qin, K. Chang, Non-lignin constructing the gas-solid interface for enhancing the photothermal catalytic water vapor splitting, Adv. Mater. 35 (45) (2023) 2305535, https://doi.org/10.1002/adma.202305535.
[44] D. Xie, M. He, X. Li, J. Sun, J. Luo, Y. Wu, F. Cheng, Tree-inspired efficient solar evaporation and simultaneous in-situ purification of ultra-highly concentrated mixed volatile organic wastewater, Nano Energy 93 (2022) 106802, https://doi.org/10.1016/j.nanoen.2021.106802.
[45] P.P. Zhang, F. Zhao, W. Shi, H.Y. Lu, X.Y. Zhou, Y.H. Guo, G.H. Yu, Super water-extracting gels for solar-powered volatile organic compounds management in the hydrological cycle, Adv. Mater. 34 (12) (2022) 2110548, https://doi.org/10.1002/adma.202110548.
[46] Y. Bao, C. Lian, K. Huang, H. Yu, W. Liu, J. Zhang, M. Xing, Generating high-valent iron-oxo $\equiv Fe^{IV}=O$ complexes in neutral microenvironments through peroxymonosulfate activation by Zn-Fe layered double hydroxides, Angew. Chem. Int. Ed. 61 (42) (2022) e202209542, https://doi.org/10.1002/anie.202209542.
[47] R. Zheng, T. Lin, W.L. Zhao, R. Yin, H. Li, Z. Deng, W. Chen, Y.F. Song, Hierarchical CoMn-LDH based photothermal membrane with low evaporation enthalpy and narrow bandgap toward highly efficient solar-driven evaporation, Chem. Eng. J. 470 (2023) 144103, https://doi.org/10.1016/j.cej.2023.144103.
[48] W. Kong, Z. Xing, B. Fang, Y. Cui, Z. Li, W. Zhou, Plasmon Ag/Na-doped defective graphite carbon nitride/NiFe layered double hydroxides Z-scheme heterojunctions toward optimized photothermal-photocatalytic-Fenton performance, Appl. Catal. B Environ. 304 (2022) 120969, https://doi.org/10.1016/j.cej.2023.144421.
[49] F. Ni, P. Xiao, N. Qiu, C. Zhang, Y. Liang, J. Gu, J. Xia, Z. Zeng, L. Wang, Q. Xue, T. Chen, Collective behaviors mediated multifunctional black sand aggregate towards environmentally adaptive solar-to-thermal purified water harvesting, Nano Energy 68 (2020) 104311, https://doi.org/10.1016/j.nanoen.2019.104311.
[50] H. Liu, B. Chen, Y. Chen, M. Zhou, F. Tian, Y. Li, J. Jiang, W. Zhai, Bioinspired self-standing, self-floating 3D solar evaporators breaking the trade-off between salt cycle and heat localization for continuous seawater desalination, Adv. Mater. 35 (24) (2023) 2301596, https://doi.org/10.1002/adma.202301596.
[51] B. Peng, Q. Lyu, M. Li, S. Du, J. Zhu, L. Zhang, Phase-separated polyzwitterionic hydrogels with tunable sponge-like structures for stable solar steam generation, Adv. Funct. Mater. 33 (18) (2023) 2214045, https://doi.org/10.1002/adfm.202214045.
[52] P. Xiao, W. Yang, N. Qiu, S. Li, F. Ni, C. Zhang, J. Gu, S.W. Kuo, T. Chen, Engineering biomimetic nanostructured "Melanosome" textiles for advanced solar-to-thermal devices, Nano Lett. 22 (23) (2022) 9343–9350, https://doi.org/10.1021/acs.nanolett.2c02385.
[53] X.M. Cui, Q.F. Ruan, X.L. Zhuo, X.Y. Xia, J.T. Hu, R.F. Fu, Y. Li, J.F. Wang, H.X. Xu, Photothermal nanomaterials: a powerful light-to-heat converter, Chem. Rev. 123 (11) (2023) 6891–6952, https://doi.org/10.1021/acs.chemrev.3c00159.
[54] Y.X. Li, Y. Ma, Y.J. Liao, L.Z. Ji, R.Z. Zhao, D.P. Zhu, X. Hu, G.W. Qin, H.W. Rong, X.F. Zhang, High-entropy-alloy-nanoparticles enabled wood, evaporator for efficient photothermal conversion and sustainable solar desalination, Adv. Energy Mater. 12 (47) (2022) 2203057, https://doi.org/10.1002/aenm.202203057.
[55] Y. Zheng, B. Cheng, W. You, J. Yu, W. Ho, 3D hierarchical graphene oxide-NiFe LDH composite with enhanced adsorption affinity to Congo red, methyl orange and Cr(VI) ions, J. Hazard. Mater. 369 (2019) 214–225, https://doi.org/10.1016/j.jhazmat.2019.02.013.
[56] C. Zhang, P. Xiao, F. Ni, J. Gu, J. Chen, Y. Nie, S.W. Kuo, T. Chen, Breathable and superhydrophobic photothermic fabric enables efficient interface energy management via confined heating strategy for sustainable seawater evaporation, Chem. Eng. J. 428 (2022) 131142, https://doi.org/10.1016/j.cej.2021.131142.
[57] X. Zhou, F. Zhao, Y. Guo, B. Rosenberger, G. Yu, Architecting highly hydratable polymer networks to tune the water state for solar water purification, Sci. Adv. 5 (6) (2019) eaaw5484, https://doi.org/10.1126/sciadv.aaw5484.
[58] Y. Lu, D. Fan, Y. Wang, H. Xu, C. Lu, X. Yang, Surface patterning of two-dimensional nanostructure-embedded photothermal hydrogels for high-yield solar steam generation, ACS Nano 15 (6) (2021) 10366–10376, https://doi.org/10.1021/acsnano.1c02578.
[59] X. Liu, F. Chen, Y. Li, H. Jiang, D.D. Mishra, F. Yu, Z. Chen, C. Hu, Y. Chen, L. Qu, W. Zheng, 3D hydrogel evaporator with vertical radiant vessels breaking the trade-off between thermal localization and salt resistance for solar desalination of high-salinity, Adv. Mater. 34 (36) (2022) 2203137, https://doi.org/10.1021/acsami.2c14773.
[60] J. Cao, S. Sun, X. Li, Z. Yang, W. Xiong, Y. Wu, M. Jia, Y. Zhou, C. Zhou, Y. Zhang, Efficient charge transfer in aluminum-cobalt layered double hydroxide derived from Co-ZIF for enhanced catalytic degradation of tetracycline through peroxymonosulfate activation, Chem. Eng. J. 382 (2020) 122802, https://doi.org/10.1016/j.cej.2019.122802.
[61] R. Guo, L. Nengzi, Y. Chen, Y. Li, X. Zhang, X. Cheng, Efficient degradation of sulfamethoxazole by CuCo LDH and LDH@fibers composite membrane activating peroxymonosulfate, Chem. Eng. J. 398 (2020) 125676, https://doi.org/10.1016/j.cej.2020.125676.
[62] C. Chen, M. Yan, Y. Li, Y. Hu, J. Chen, S. Wang, X.L. Wu, X. Duan, Single-atom co sites confined in layered double hydroxide for selective generation of surface-bound radicals via peroxymonosulfate activation, Appl. Catal. B Environ. 340 (2024) 123218, https://doi.org/10.1016/j.apcatb.2023.123218.
[63] Y. Deng, J. Wang, J. Wang, H. Zhang, H. Xiao, C. Zhang, W. Wang, In situ growth of Bi/Ag double quantum dots on hollow Bi_2MoO_6 microspheres: enhancement of the surface plasmon resonance effect on PMS activation, Appl. Catal. B Environ. 338 (2023) 123041, https://doi.org/10.1016/j.apcatb.2023.123041.
[64] T. Li, M. Li, J. Jiang, Z. Zhao, Z. Li, C. Zhao, X. Wang, S. Dong, Bimetallic (Cu, Zn) ZIF-derived S-scheme heterojunction for efficient remediation of aqueous pollutants in visible light/ peroxymonosulfate system, Appl. Catal. B Environ. 330 (2023) 122539, https://doi.org/10.1016/j.apcatb.2023.122539.
[65] Z. Wang, R. Jin, S. Zhang, X. Han, P. Guo, L. Jiang, L. Heng, Bioinspired, sustainable, high-efficiency solar evaporators for sewage purification, Adv. Funct. Mater. 33 (47) (2023) 2306806, https://doi.org/10.1002/adfm.202306806.
[66] H. Bai, P. He, L. Hao, Z. Fan, R. Niu, T. Tang, J. Gong, Waste-treating-waste: upcycling discarded polyester into metal-organic framework nanorod for synergistic interfacial solar evaporation and sulfate-based advanced oxidation process, Chem. Eng. J. 456 (2023) 140994, https://doi.org/10.1016/j.cej.2022.140994.
[67] B. Lv, S. Li, W. Wang, Y. Xu, B. Zhao, C. Song, X. Fan, Y. Liu, A lotus leaf-inspired Janus dual-functional nanofiber evaporator for efficient water purification, J. Clean. Prod. 438 (2024) 140880, https://doi.org/10.1016/j.jclepro.2024.140880.
[68] Z. Fan, P. He, H. Bai, J. Liu, H. Liu, L. Liu, R. Niu, J. Gong, Green recycling of waste poly(ethylene terephthalate) into NI-MOF nanorod for simultaneous interfacial solar evaporation and photocatalytic degradation of organic pollutants, EcoMat 6 (2024) e12422, https://doi.org/10.1002/eom2.12422.